ACS APPLIED MATERIALS & INTERFACES

Research Article

www.acsami.org

Heterojunction of Zinc Blende/Wurtzite in $Zn_{1-x}Cd_xS$ Solid Solution for Efficient Solar Hydrogen Generation: X-ray Absorption/Diffraction Approaches

Ying-Ya Hsu,[†] Nian-Tzu Suen,[‡] Chung-Chieh Chang,[§] Sung-Fu Hung,[‡] Chi-Liang Chen,[*,§,∥] Ting-Shan Chan,[*,∥] Chung-Li Dong,[⊥] Chih-Chieh Chan,[#] San-Yuan Chen,[△,∥] and Hao Ming Chen[*,‡]

[†]Program for Science and Technology of Accelerator Light Source and [△]Department of Materials Science and Engineering, National Chiao Tung University, Hsinchu 300, Taiwan

[‡]Department of Chemistry, National Taiwan University, Taipei 106, Taiwan

[§]Institute of Physics, Academia Sinica, Taipei 115, Taiwan

[∥]National Synchrotron Radiation Research Center, Hsinchu Science Park, Hsinchu 300, Taiwan

[⊥]Department of Physics, Tamkang University, Tamsui 251, Taiwan

[#]Department of Chemical Engineering, Feng-Chia University, Taichung 407, Taiwan

Supporting Information

ABSTRACT: In the past decade, inorganic semiconductors have been successfully demonstrated as light absorbers in efficient solar water splitting to generate chemical fuels. Pseudobinary semiconductors $Zn_{1-x}Cd_xS$ ($0 \le x \le 1$) have exhibited a superior photocatalytic reactivity of H_2 production from splitting of water by artificial solar irradiation without any metal catalysts. However, most studies had revealed that the extremely high efficiency with an optimal content of $Zn_{1-x}Cd_xS$ solid solution was determined as a result of elevating the conduction band minimum (CBM) and the width of bandgap. In addition to corresponding band structure and bandgap, the local crystal structure should be taken into account as well to determine its photocatalytic performance. Herein, we demonstrated the correlations between the photocatalytic activity and structural properties that were first studied through synchrotron X-ray diffraction and X-ray absorption spectroscopy. The crystal structure transformed from zinc blende to coexisted phases of major zinc blende and minor wurtzite phases at a critical point. The heterojunction formed by coexistence of zinc blende and wurtzite phases in the $Zn_{1-x}Cd_xS$ solid solution can significantly improve the separation and migration of photoinduced electron−hole pairs. Besides, X-ray absorption spectra and UV−vis spectra revealed that the bandgap of the $Zn_{0.45}Cd_{0.55}S$ sample extended into the region of visible light because of the incorporation of Cd element in the sample. These results provided a significant progress toward the realization of the photoelectrochemical mechanism in heterojunction between zinc blende and wurtzite phases, which can effectively separate the charge-carriers and further suppress their recombination to enhance the photocatalytic reactivity.

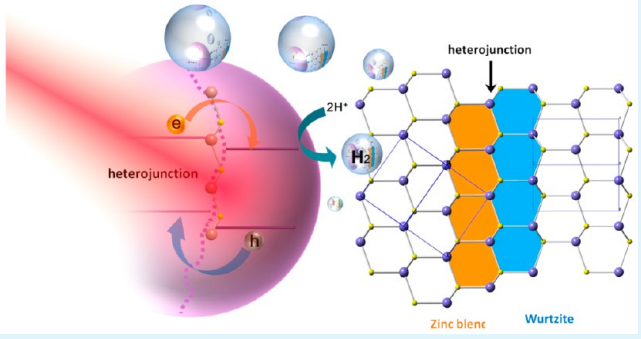

KEYWORDS: *hydrogen evolution reaction (HER), zinc−cadmium sulfide, heterojunction, X-ray absorption, density of states (DOS) and Rietveld structural refinements*

INTRODUCTION

Over the past century, the growing energy demand and environmental problem have become more apparent on a global scale. Acquiring renewable energy resources and conversion pathways to substitute fossil fuel is an essential and challenging issue. Among various solutions, hydrogen generation from photocatalytic water splitting under solar illumination serves a promising route for generation of clean energy. Numerous attempts have been demonstrated to design and to synthesize photocatalysts with suitable bandgaps to produce hydrogen. Among hundreds of candidates that including inorganic compounds and semiconductors, cadmium sulfide (CdS) and zinc sulfide (ZnS) have attracted much interest because of their interesting optical and electronic properties (quantum size effect) as well as their potential applications in optoelectronic devices and photovoltaic cells.[1−3] CdS exhibits excellent properties in photocatalytic hydrogen production because its bandgap corresponds well to the visible

Received: July 28, 2015
Accepted: September 24, 2015
Published: September 24, 2015

DOI: 10.1021/acsami.5b06872
ACS Appl. Mater. Interfaces 2015, 7, 22558−22569

region of the solar spectrum.[4,5] Several research groups have demonstrated that by mixing CdS with other semiconductors, it could further improve the efficiency of the hydrogen production.[6−9] However, it lacks stability to resist the undesired photocorrosion and therefore it is essential to embed CdS in mesoporous materials or polymer matrix to form hybrid photocatalysts, which can remarkably protect CdS from photocorrosion.[10,11] On the other hand, ZnS is a well-known photocatalyst with wide bandgap (3.6 eV) and high negative potential of excited electrons, which allows to produce hydrogen gas from water without any assistance of noble metal as cocatalysts.[12] Furthermore, various groups have studied the synthesis of high-quality $Zn_{1-x}Cd_xS$ nanocrystals with high photoluminescence properties and extremely narrow spectra.[13,14] Moreover, these studies have revealed that this pseudobinary ($Zn_{1-x}Cd_xS$) system possessed tunable compositions as well as optical and electric properties, therefore this system has great potential application in photocatalysis, high density optical recording, and blue or ultraviolet laser diodes.[15−17] Although the doping treatment is expected to significantly improve the absorption of visible light, the efficient doped ZnS photocatalysts under visible light have not been achieved yet.

In terms of material design, a solid-solution nanocomposite formed by wide and narrow bandgap semiconductors can adjust their bandgap width through forming a newly orbital hybridization of atoms.[18−20] The newly formed energy band in $Zn_{1-x}Cd_xS$ material could respond to visible light, once CdS and ZnS are able to form a solid solution with a narrow bandgap.[21] Studies on activity of solar hydrogen generation over $Zn_{1-x}Cd_xS$ solid solution have revealed the importance of tuning band edges and electronic properties in the control of changing their constituent stoichiometries between CdS and ZnS materials,[22] and thereby it can be regarded as an excellent candidate for visible-light-driven photocatalytic water splitting.[23] Furthermore, more negative reduction potential of the conduction band in $Zn_{1-x}Cd_xS$ can result in more efficient hydrogen production than that of CdS. A remarkable improvement of photoactivity had been obtained for solid solution of $Zn_{1-x}Cd_xS$ from the thermal treatment at 1073 K, whereas the $Zn_{1-x}Cd_xS$ solid solution exhibited a higher crystallinity of hexagonal phase and less Cd sublimation which decreased the generation of structural defects and the quantity component of Cd over $Zn_{1-x}Cd_xS$ solid solution with hexagonal phase exhibits the highest photocatalytic activity.[24,25] As a result, in addition to the tuning of band edge position, the photocatalytic hydrogen generation can be significantly enhanced by the formation of twin structures that it can effectively separate the charge-carriers to suppress the recombination probability. Although several results indicated that the $Zn_{1-x}Cd_xS$ with hexagonal phase exhibited the highest efficiency. Wang et al. have shown that $Cd_{0.44}Zn_{0.56}S$ possessed more vigorous reactivity of hydrogen evolution with cubic phase[26] while the electron transfer properties along the direction parallel to (111) in the zinc blende structure were considerably more effective than that of (001) plane within hexagonal structure. Therefore, the photocatalytic activity with an optimum composition of $Zn_{1-x}Cd_xS$ is not only dependent on the electronic band structure but also the local crystallite and morphology. Because the conventional solid solution was prepared by mixing heterogeneous photocatalysts at extremely high temperature while no heterojunctions were formed in between. Few works have been achieved at low-temperature synthesis routes of $Zn_{1-x}Cd_xS$ nanocrystals that were regarded as solid solution for photocatalytic hydrogen evolution.[26,27] The minor cations of $Zn_{1-x}Cd_xS$ solid solutions substituted the cations of the major component in the zinc blende phase and hold the Vegard's law in these studies.[28] However, it was difficult to achieve a considerable correlation between the photocatalytic activities of hydrogen production with a low temperature synthesis and their corresponding crystal phase. As a result, to achieve a perfect photocatalyst, electronic band structure (bandgap) and heterojunction with heterocrystal have to be simultaneously considered.[29,30] Moreover, the heterojunction formation between two boundaries can be expected to significantly promote the transport nature and separation efficiencies of photogenerated electron−hole pairs.[31]

Herein, we demonstrated a low temperature approach of systematic synthesizing $Zn_{1-x}Cd_xS$ ($0 \le x \le 1$) nanocomposites with heterojunctions in between. Furthermore, it can act as a model system to study the correlation between photocatalytic activities of hydrogen production and their corresponding crystal phases by employing synchrotron X-ray diffraction (XRD) and X-ray absorption spectroscopy (XAS). We can well study the practically dominated factors of local structure and electronic properties in the $Zn_{1-x}Cd_xS$ photocatalytic system; the bowing effect allows us to systematically realize the heterojunction effects that play dominant roles in raising photogenerated carriers transportation and separation. In addition, density functional theory (DFT) calculation that can provide theoretical approaches to their band structure is demonstrated for comparison with experimental results as well. Consequently, these complementary approaches are utilized in the present study to systematically realize the dominative factors, and further provide a fundamental strategy to the design of solar energy utilization.

EXPERIMENTAL SECTION

Preparation of Photocatalysts. A series of $Zn_{1-x}Cd_xS$ nanocomposites was synthesized via the simple coprecipitation method. First, a solution of 1.0 M $Zn(CH_3COO)_2$ and $Cd(CH_3COO)_2$ was prepared by dissolving $0.1 \times (1 - x)$ mole ($0 \le x \le 1$) of $Zn(CH_3COO)_2{\cdot}2H_2O$ and 0.1 x mole of $Cd(CH_3COO)_2{\cdot}2H_2O$ in 100 mL of deionized water. Then, 100 mL of 1.0 M Na_2S aqueous solution was added into the mixture solution of $Zn(CH_3COO)_2$ and $Cd(CH_3COO)_2$ with vigorous stirring. The reaction was further conducted for 30 min under ambient condition. The resulting yellow slurry was centrifuged, washed several times, and then dried in the oven under 80 °C for 24 h. The as-prepared $Zn_{1-x}Cd_xS$ powders were ground in the mortar before further use.

Characterization of Nanocomposites. The morphology and energy-dispersive spectroscopy (EDS) element mapping of $Zn_{1-x}Cd_xS$ samples were observed by using a field-emission scanning electron microscopy (SEM, JEOL, JSM-7600F) with accelerated voltage of 10 kV and secondary electron detector. TEM and HRTEM images were collected by using a transmission electron microscope (TEM, Hitachi, H-7650) and a high-resolution transmission electron microscope (HRTEM, JEOL, JEM-2100F) with working voltages of 100 kV and 200 kV, respectively. The crystallographic structures of $Zn_{1-x}Cd_xS$ samples were analyzed by X-ray powder diffraction (XRD) with Cu Kα radiation (λ = 0.154056 nm). The surface chemical compositions and speciation on the catalysts were examined by X-ray Photoelectron Spectroscopy (XPS, PHI Quantera SXM) using an ion gun beam. The elemental analysis was also carried out on an inductively coupled plasma mass spectrometry (ICP-MS, PerkinElmer, ELAN 6000). A diffuse reflectance UV−vis spectrophotometer (JASCO, V-670) was used to characterize the absorption properties of the catalysts. The bandgap of catalysts was determined from the absorption edges that converted from the reflectance spectra via Kubelka−Munk equation.

DOI: 10.1021/acsami.5b06872
ACS Appl. Mater. Interfaces 2015, 7, 22558−22569

X-ray Absorption/Diffraction Analysis. The phase purity of the synthesized samples was determined by PXRD analysis (λ = 0.774908 Å) using a large Debye−Scherrer camera that was installed at beamline BL01C2 at the National Synchrotron Radiation Research Center (NSRRC), Taiwan. The electron storage ring was operated at 1.5 GeV and the current was 360 mA. The GSAS program was used to elucidate the crystal structure.[32] X-ray absorption spectroscopy including X-ray absorption near edge spectra (XANES) and extended X-ray absorption fine structural (EXAFS) spectra at the S, Zn and Cd *K*-edges were recorded in total-fluorescence-yield (TFY) mode at beamlines BL16A and transition mode at beamline BL01C1 for powdered samples. The XANES spectra at the S $L_{2,3}$-edges were obtained at BL20A as a high energy spherical grating monochromator (HSGM) beamline in a total-electron-yield (TEY) mode. The characteristic pre-edge absorption of metallic foil were determined from the peaks in the first derivative XANES after subtraction of postedge baseline and normalization to the edge jump were used for calibration of energy shifts at 9659.0 and 26711.0 eV, respectively. EXAFS analyses were conducted by using an analytical package called "Artemis", and Fourier transformation was carried out on k^3-weighted EXAFS oscillations toward Zn and Cd species at k range of 3.59−12.22 and 3.46−11.97 Å^{-1}, respectively, to evaluate the contribution of each bond pair to the Fourier transform (FT) peak.

Photocatalytic Reaction. A batch system with a cylindrical quartz tube was designed for the photocatalytic H_2 evolution. The photocatalyst powder of approximately 1 mg was dispersed in 3 mL of aqueous solution containing 0.25 M Na_2S and 0.35 M K_2SO_3 as electron donors. The photocatalysts were irradiated by an irradiation of 300 mW/cm^2 from Xe lamp (Newport Oriel, 91160) with long-pass filters (λ > 400 nm). During the irradiation, the mixture was suspended vigorously by using a magnetic stirrer. The gaseous product was transported through a stainless steel tube to gas chromatography (GC) by high negative pressure at the end of pipe. It is finally measured by using GC (Angilent Technologies, 7890B) equipped with a capillary column (30 m × 0.53 mm, HP-PLOT Molesieve), a thermal couple detector (TCD) and a flame ionization detector (FID).

Photoelectrochemical Measurement. Photoelectrochemical experiments were performed in CHI-704E potentiostat (CH Instruments, Inc.). All potentials were referenced to platinum plate as the counter electrode and an Ag/AgCl (3 M NaCl) electrode as the reference electrode, in which the electrolyte was used 0.25 M Na_2S and 0.35 M K_2SO_3 solution. For visible-light measurement, a 400 nm long pass filter was attached to the light source of 300 mW/cm^2 Xe lamp. The open-circuit voltage decay (OCVD) measurements were obtained to study the assumption that the charge recombination. The electrochemical impedance spectroscopy (EIS) was performed under visible light illumination (λ > 400 nm) in a frequency range from 0.1 to 1 × 10^5 Hz with an AC amplitude of 5 mV.

Electronic Structure Calculation. To have better understanding of incorporating Cd element in the $Zn_{1-x}Cd_xS$ series and the effect of heterojunction between zinc blende (cubic structure) and wurtzite (hexagonal sturcutre) phases, the electronic structures of hypothetical ordered ternary zinc blende phases ZnS, $Zn_{0.75}Cd_{0.25}S$, $Zn_{0.5}Cd_{0.5}S$, $Zn_{0.25}Cd_{0.75}S$, CdS, and wurtzite phase $Zn_{0.5}Cd_{0.5}S$ were computed with the Stuttgart TB-LMTO 4.7 program. The total and partial density of states (DOS) curves were present and discussed. The symmetry of the potential is considered spherical and the combined correction was used to handle the overlapping part within each Wigner−Seitz (WS) sphere. Local density approximation (LDA) was used to deal the exchange and correlation terms. The radii of WS spheres were determined by default as follows: Zn = 1.39−1.56 Å; Cd = 1.50−1.58 Å; S = 1.46−1.52 Å. The basis sets included 4s, 4p, 3d orbitals for Zn; 5s, 5p, 4d and 4f orbital for Cd; 3s, 3p, and 3d orbitals for S. The tetrahedron method was utilized to process the integrations in k space. The self-consistent charge density was satisfied with more than 100 irreducible k-points in the Brillouin zone for all cases.

RESULTS

Crystal Structure and Morphology Characterizations. A series of $Zn_{1-x}Cd_xS$ compounds ($0 \le x \le 1$) have been synthesized at low temperature (80 °C), and their structures have been characterized with the powder X-ray diffraction (PXRD) technique by using synchrotron light source and shown in Figure 1. Three distinctive diffraction peaks were

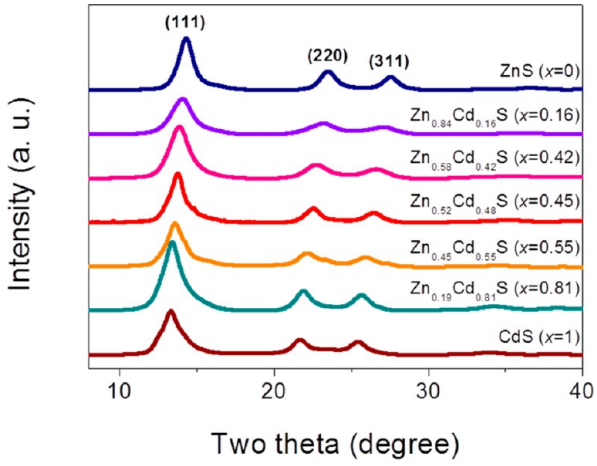

Figure 1. Synchrotron PXRD patterns of $Zn_{1-x}Cd_xS$ samples with various x values.

detected in all compounds that could be referred to the (111), (220), and (311) facets, indicating that the primary phase in $Zn_{1-x}Cd_xS$ series was zinc blende phase. With more careful examination of the XRD, it was realized that the width of all diffraction peaks gradually became broad with increasing of Cd amount, which could be attributed to decreasing the crystalline size. However, the discrepancy of crystal size among all samples was not significant (as shown in Table S1). More importantly, XRD patterns of the $Zn_{1-x}Cd_xS$ samples in the case of $x \ge 0.48$ exhibited additional peaks that were clearly suggesting the existence of phases other than zinc blende phase in the samples. To obtain more detail information for the structural evolution and crystal structures of $Zn_{1-x}Cd_xS$ ($0 \le x \le 1$) pseudobinary system, we utilized Rietveld structural refinements to refine all samples and the result was plotted in Figure 2. In Figure 2a−d, the refinements for $Zn_{1-x}Cd_xS$ in the case of $x \le 0.42$ confirmed that within this range, the $Zn_{1-x}Cd_xS$ samples are indeed solid solution with zinc blende phase (space group: $F\bar{4}3m$). Once the Cd content was further increased to the level of $x \ge 0.48$, the resulting crystal structure became considerably distorted and formed mixed phases, in which a minor wurtzite phase (space group: $P6_3mc$) was observed (as displayed in Figure 2e, f). Tables S1 and S2 present the final structural parameters of $Zn_{1-x}Cd_xS$ ($0 \le x \le 1$) with the zinc blende and wurtzite phases, respectively. Notice that the radius of Cd^{2+} ions is 0.78 Å (coordination number: CN = 4) and that of Zn^{2+} ions is 0.60 Å (CN = 4),[33] suggested that substitution of a larger Cd^{2+} ions should led to a significant increase in unit cell parameters. As seen in Tables S1 and S2, the unit-cell parameters, volumes, and Zn/Cd−S bond lengths increased monotonically with increasing Cd content in the samples as expected. The Zn/Cd−S average bond lengths determined from Rietveld refinements for $Zn_{1-x}Cd_xS$ in zinc blende phase varied from 2.334 to2.531 Å (Table S1), and the mean of two wurtzite bond lengths increased from 2.458 Å in the

DOI: 10.1021/acsami.5b06872
ACS Appl. Mater. Interfaces 2015, 7, 22558−22569

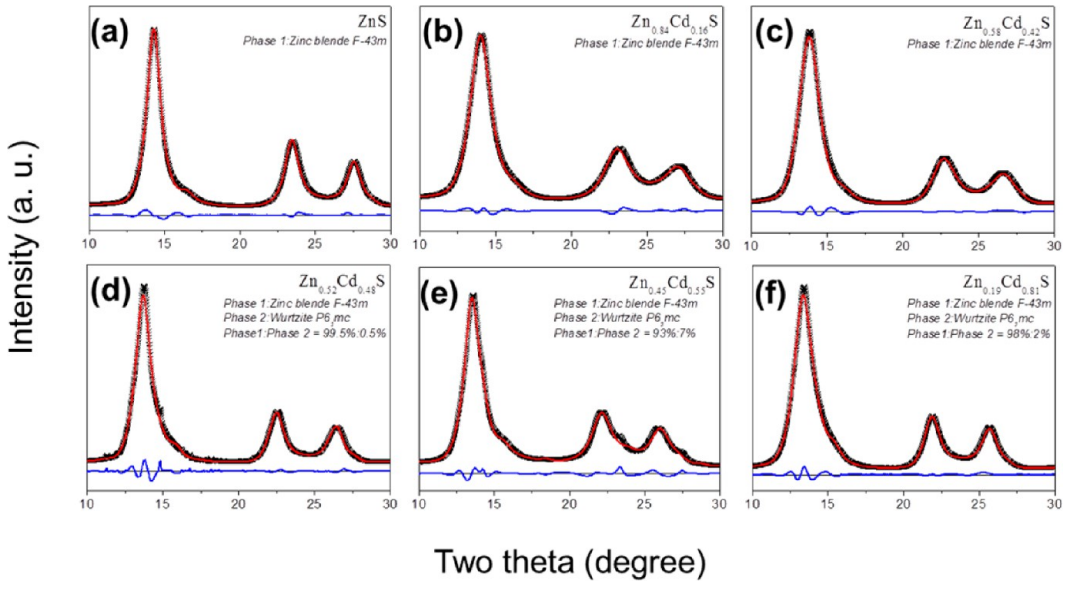

Figure 2. PXRD profiles of various $Zn_{1-x}Cd_xS$ samples with x = (a) 0, (b) 0.16, (c) 0.42, (d) 0.48, (e) 0.55, and (f) 0.81, in which observed (crosses), calculated (solid line), and differences (bottom) are plotted and Bragg reflections are indicated by tick marks.

Table 1. Structural Parameters from Both Zn *K*-Edge and Cd *K*-Edge EXAFS Fitting for Various $Zn_{1-x}Cd_xS$ Samples[a]

	ZnS	$Zn_{0.84}Cd_{0.16}S$		$Zn_{0.58}Cd_{0.42}S$		$Zn_{0.52}Cd_{0.48}S$		$Zn_{0.45}Cd_{0.55}S$		$Zn_{0.19}Cd_{0.81}S$		CdS
shell	Zn−S	Zn−S	Cd−S	Zn−S	Cd−S	Zn−S	Cd−S	Zn−S	Cd−S	Zn−S	Cd−S	Cd−S
N	3.6	2.8	4.2	2.8	3.2	2.8	4.2	3.2	3.5	3.5	3.8	3.9
R (Å)	2.331	2.340	2.519	2.345	2.527	2.356	2.534	2.343	2.527	2.343	2.538	2.534
R_{ave} (Å)	2.331	2.369		2.421		2.441		2.444		2.501		2.534
σ^2 (Å^2)	0.009	0.006	0.009	0.006	0.005	0.004	0.006	0.008	0.006	0.009	0.007	0.008
ΔE_0 (eV)	1.86	4.46	0.48	4.65	3.85	4.85	6.98	3.19	2.82	4.10	4.70	3.54

[a]Variable: N, coordination number R, bonding distance; R_{ave}, Zn/Cd−S average bond length; σ^2, Debye−Waller factor; and ΔE_0, inner potential shift.

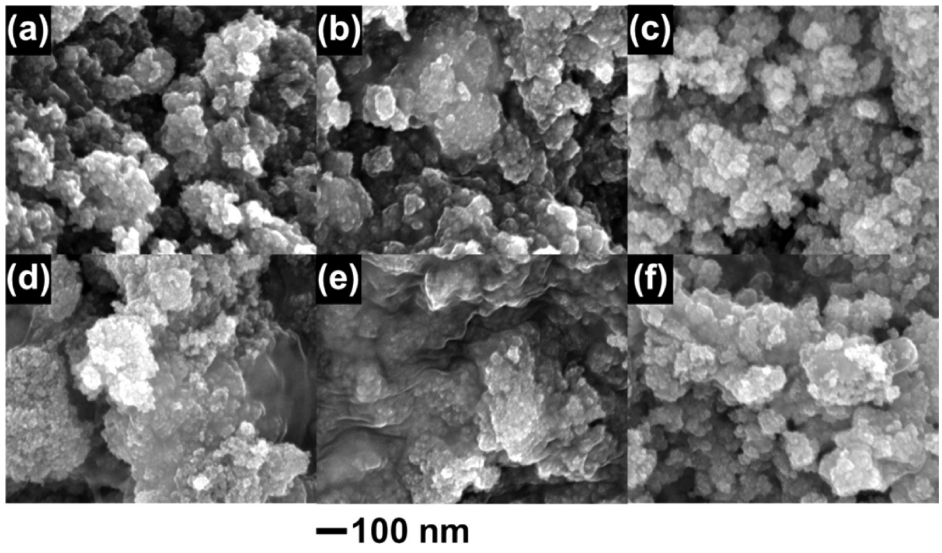

Figure 3. SEM images of the $Zn_{1-x}Cd_xS$ samples with various x values: (a) 0, (b) 0.16, (c) 0.42, (d) 0.48, (e) 0.55, and (f) 0.81.

$Zn_{0.48}Cd_{0.52}S$ to 2.534 Å in the case of CdS. It is worth mentioning that there is a "jump" in bond lengths of Zn/Cd−S, which increased nonlinearly at the point where minor wurtzite phase appeared ($Zn_{0.45}Cd_{0.55}S$). Consequently, a homogeneous structure was clarified through the Rietveld refinement while the lattice parameters of $Zn_{1-x}Cd_xS$ solid solution were consistent with Vegard's law,[34] which a linear change of bandgaps of $Zn_{1-x}Cd_xS$ should be expected. Moreover, Rietveld refinement also revealed that the wurtzite phase existed in $Zn_{1-x}Cd_xS$ ($x \geq 0.48$), which implies the possible formation of heterojunction between these two phases (i.e., zinc blende and wurtzite phases) in the present system.

DOI: 10.1021/acsami.5b06872
ACS Appl. Mater. Interfaces 2015, 7, 22558−22569

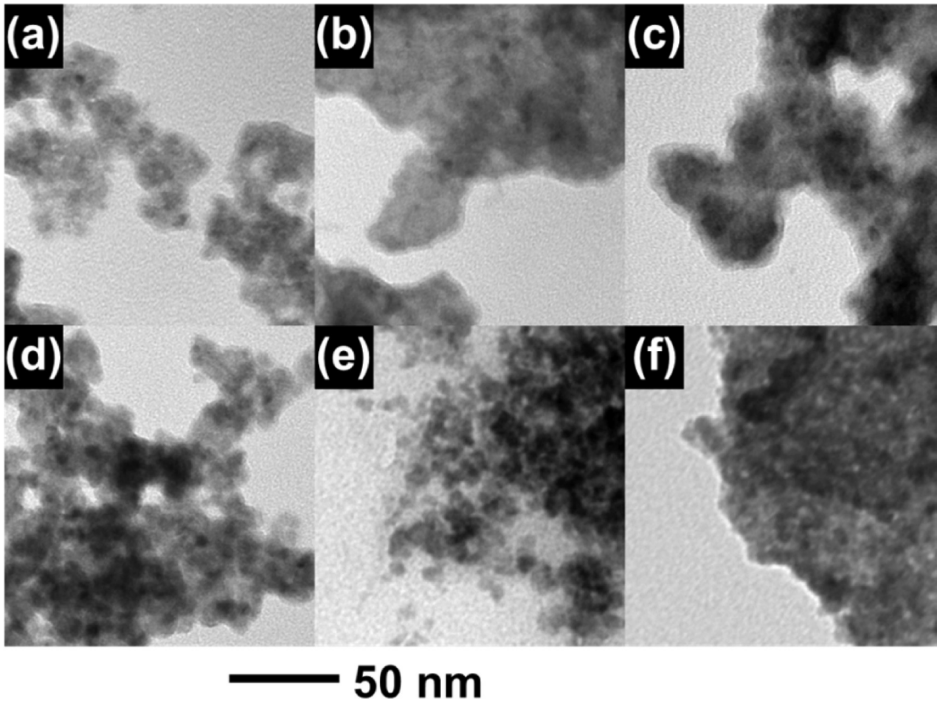

Figure 4. TEM images of the $Zn_{1-x}Cd_xS$ samples with various x values: (a) 0, (b) 0.16, (c) 0.42, (d) 0.48, (e) 0.55, and (f) 0.81.

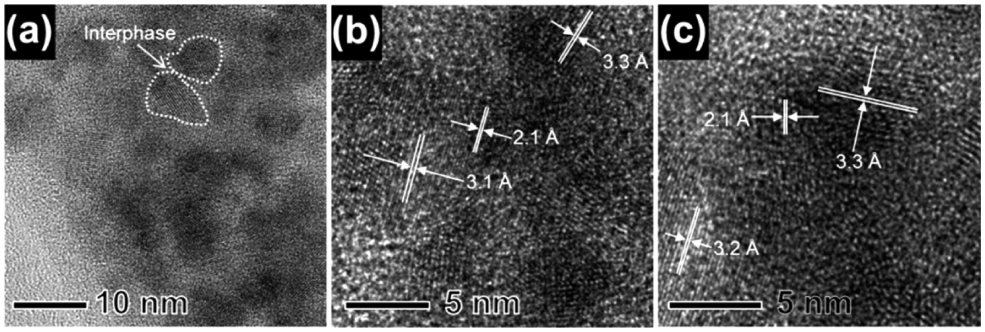

Figure 5. HR-TEM images of the $Zn_{0.52}Cd_{0.48}S$ sample: (a) the area of white dashed circle shows the local structure in a crystal; (b) a mixed zinc blende and wurtzite phases stacking in a sample; (c) the interplanar spacings of wurtzite (101) and (220) facet are 3.2 and 2.1 Å, respectively.

It was noteworthy that the bond lengths of Zn/Cd−S derived from Rietveld refinement across the whole series ($Zn_{1-x}Cd_xS$; $0 \le x \le 1$) are the result of average bond lengths of Zn−S and Cd−S, which cannot reflect the real case of individual Zn−S and Cd−S bonds. Take $Zn_{0.52}Cd_{0.48}S$ for instance, the bond length of Zn/Cd−S is 2.426(7) Å that is considerably longer than the sum of covalent radii of Zn and S (d_{Zn-S} = 2.27 Å) and yet much shorter than the sum of Cd and S (d_{Cd-S} = 2.49 Å). To have more understanding of the local crystal structure on individual elements in this system, the X-ray absorption spectroscopy measurements using synchrotron radiation were carried on all samples. X-ray absorption spectroscopy is a powerful technique to investigate the local structural details and electronic properties of the X-ray absorbing atoms and its local environment. Structural parameters were obtained from the fitting of the Fourier transformed (FT) EXAFS spectra. The peaks of FT-EXAFS contained many contributions from both single and multiple scattering paths and they were fitted with a single set of distances (R) and Debye−Waller factors (σ^2) and then float the energy zero (e_0) to calculate the coordination numbers (N). Table 1 and Figure S4 present the parameters and amplitudes of the fitted k^3-weighted FT-EXAFS results. The peak centered at about 2.4 Å in the FT spectra for these materials, which resulted from the single scattering paths of first shells of Zn−S and Cd−S coordination bonds. The refined bond lengths of Zn−S and Cd−S from EXAFS results slightly increase while Cd content (x) increase. In general, they are in good agreement with the sum of covalent radii of corresponding elements. Moreover, the averaged Zn−S and Cd−S bond lengths are incredibly comparable to those derived from Rietveld refinement.

Along this line of thinking, it is necessary to examine the morphology of $Zn_{1-x}Cd_xS$ samples to have better understanding of their nanostructures. As seen from scanning electron microscope (SEM; Figure 3) and transmission electron microscope (TEM; Figure 4), the morphology and the nanostructure of a series of $Zn_{1-x}Cd_xS$ ($0 \le x \le 1$) samples were composed of aggregated tiny nanoparticles. Figure S5 shows representative X-ray elemental maps of all elements, that is, sulfur, cadmium and zinc, indicating that a homogeneous distribution of the elements is confirmed by SEM/EDS in the

DOI: 10.1021/acsami.5b06872
ACS Appl. Mater. Interfaces 2015, 7, 22558−22569

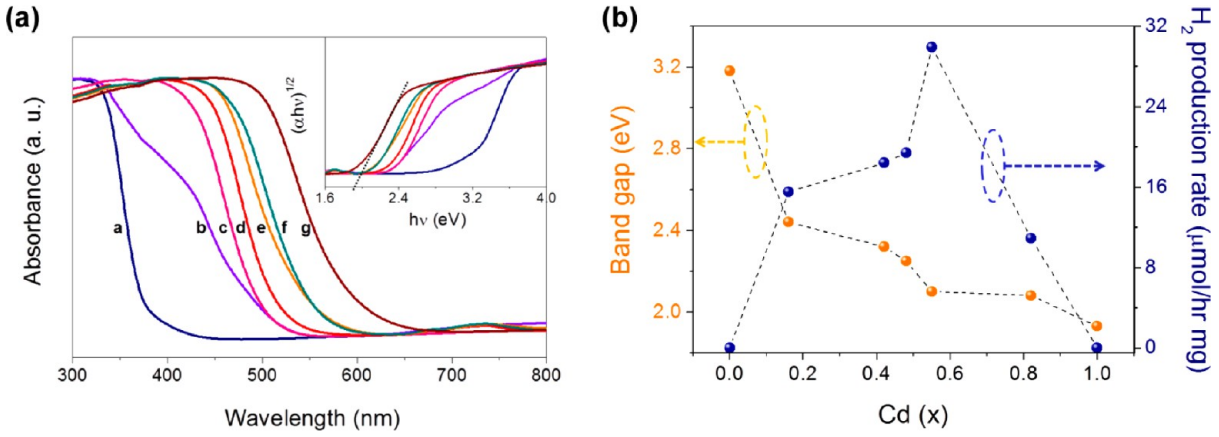

Figure 6. (a) UV−vis absorption spectra of $Zn_{1-x}Cd_xS$ samples with various x values: (a) 0, (b) 0.16, (c) 0.42, (d) 0.48, (e) 0.55, (f) 0.82, and (g) 1.0; inset is the plot of $(\alpha h\nu)^2$ vs $h\nu$. (b) Generation rate of H_2 evolution (blue circles) and the bandgap as functions of Cd concentration (x) in $Zn_{1-x}Cd_xS$ samples (orange circles).

microstructure. In the sample of ZnS, SEM (Figure 3a) and TEM images (Figure 4a) showed that the average diameter of aggregated nanoparticles was below 50 nm with irregular morphology. Introducing Cd resulted in a fact that the individual $Zn_{1-x}Cd_xS$ nanocrystals were zinc blende with mixed phases (i.e., zinc blende and wurtzite phases). As the Cd content increased (≥0.48), the dark spherical particles with distinct contrast became more apparent, which can be attributed to the discrepance in electron scattering nature caused by crystal structure and atomic scattering factor and further revealed that heterojunctions between Zn blende and wurtzite phases were formed in these sample (as shown in Figure 4c−f). To further verify this conjecture, we employed high-resolution TEM (HR-TEM) to analyze the local heterojunction structure. The HR-TEM image of $Zn_{0.52}Cd_{0.48}S$ sample was shown in Figure 5a, in which various lattice fringes with different orientations revealed that these nanoparticles have characteristic of poly crystalline in nature and exhibited randomly orientations. Magnified HR-TEM images were shown in Figure 5b, c, the $Zn_{0.52}Cd_{0.48}S$ sample was composed of numerous grains with apparent light contrast in single particle, which corroborated the conjecture that many heterojunctions existed within the particle. In this heterojunction structure, the dark region revealed a interplanar spacing of 3.3 Å which was close to the value of zinc Blende phase for $Zn_{0.52}Cd_{0.48}S$ (111) facet and Wurtzite for (002) facet,[35] meant that it was difficult to distinguish this mixed phases by electron microscope. On the contrary, the bright region in HR-TEM image showed clear crystal lattice fringes with d-spacing measured to be 3.2 and 2.1 Å which were well matched with the values of (101) and (220) facet in wurtzite phase, respectively.[36] It has to be noted that only local structurally analysis can be achieved in electron microscope even if electron energy loss spectroscopy (EELS) was employed. However, the photocatalytic performance was strongly depended on the assembly nature of photocatalysts rather than local properties, and thereby development of assembly measurement for photocatalysts in spatial distribution of zinc blende and wurtzite phases within the $Zn_{1-x}Cd_xS$ system is essential to achieve a fair evaluation of photocatalytic performance.

Table S3 summarizes the chemical analysis of a series of $Zn_{1-x}Cd_xS$ samples, in which bulk elemental composition was measured by ICP-MS and surface homogeneity was obtained from EDS. The element compositions of $Zn_{1-x}Cd_xS$ samples were obtained by EDS and ICP-MS analyses and the Zn/Cd ratios are in good agreement with stoichiometry. The surface chemical compositions and chemical states of $Zn_{1-x}Cd_xS$ samples were characterized using XPS. Figure S6 shows the analysis results of wide range scanned spectra and high resolution scanned spectra, in which all of the peaks on the curve can be ascribed to S(2p), Cd(3d), and Zn(2p). The position of Zn 2p peaks located at 1044.7 and 1021.6 eV exhibit a peak separation of 23.1 eV which suggests the presence of Zn^{2+}. The Cd 3d spectra at 405.3 and 412.1 eV exhibit a peak separation of 6.8 eV consistent with the presence of Cd^{2+}. The S 2p spectra at about 161.9 and 163.1 eV give two separate peaks of 1.2 eV, which is attributed to the S ions coordinated to metal ions or the chemically bound thiolate sulfur.[37]

UV−Vis and X-ray Absorption Spectrum Analysis. To further understand the transfer pathway of the photogenerated charge-carriers in $Zn_{1-x}Cd_xS$ compounds, the UV−vis and X-ray absorption measurements were carried out to investigate the band edges and optical properties of those compounds. The absorption edges of $Zn_{1-x}Cd_xS$ ($0 \le x \le 1$) samples were red-shifted with increasing Cd amount, and the corresponding color gradually changed from white to reddish orange between ZnS and CdS (Figure 6a). This observation also supported by the electronic structure calculation that the bandgaps of $Zn_{1-x}Cd_xS$ ($0 \le x \le 1$) samples shrunk while Cd content increased in $Zn_{1-x}Cd_xS$ ($0 \le x \le 1$) compounds.[38] To precisely determine the bandgap of $Zn_{1-x}Cd_xS$ samples, the plots of Kubelka−Munk function versus energy of the incident light were shown in the inset of Figure 7a, in which the bandgap of ZnS to CdS were determined to be 3.2 and 1.9 eV, respectively. This observation was consistent with that of pervious report, which demonstrated that formation of a ZnS-CdS solid solution could significantly improve the light absorption in the photocatalytic reaction.[39,40] Accordingly, the incorporation of Cd in the $Zn_{1-x}Cd_xS$ ($0 \le x \le 1$) system was advantageous for achieving the light absorption shift to the visible region. Besides, the formation of heterojunctions between zinc blende and wurtzite phases and small particle size could lead to a shorter diffusion length (quantum confinement), which considerably increased the separation of photogenerated charge-carriers and therefore improved catalytic performance of $Zn_{1-x}Cd_xS$ samples. As illustrated in Figure 6b, both ZnS and CdS have no activities in photocatalytic H_2 evolution. No

DOI: 10.1021/acsami.5b06872
ACS Appl. Mater. Interfaces 2015, 7, 22558−22569

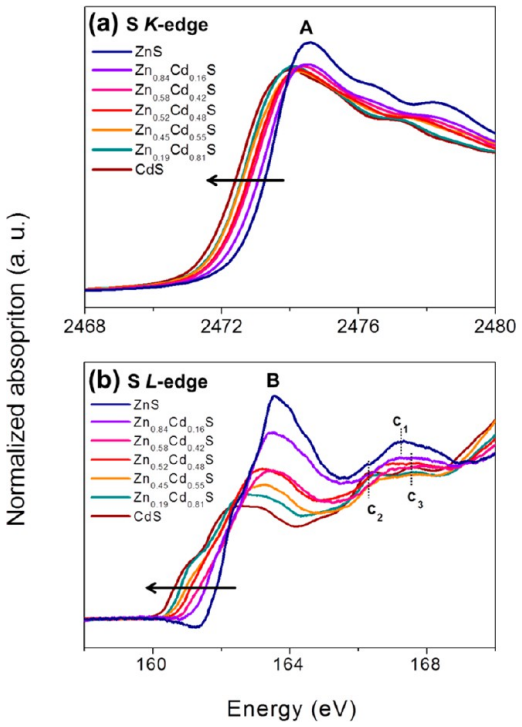

Figure 7. XANES spectra of (a) K-edge and (b) L-edge for various $Zn_{1-x}Cd_xS$ sample with x values of 0, 0.16, 0.42, 0.48, 0.55, 0.81, and 1.

hydrogen production was detected in ZnS sample owing to the limited absorption in visible light illumination, suggesting that ZnS sample was inactive under visible light for photocatalytic H_2 evolution. It was well-known that bare CdS was unstable against photocorrosion and/or photodecomposition, in which the CdS might be oxidized into Cd^{2+} and S ions by photogenerated holes,[41] and thereby a sacrificial reagent act as electron donor was utilized here to suppress these undesired effects. All $Zn_{1-x}Cd_xS$ ($0 \leq x \leq 1$) compounds exhibited remarkably higher photocatalytic activity of H_2 generation than both ZnS and CdS. In particular, $Zn_{0.45}Cd_{0.55}S$ sample performed a highest photocatalytic reactivity of generation rate of hydrogen production that it reached to the number approximately 30 μmol h^{-1} mg^{-1} under the artificial solar irradiation. Generally, a narrow bandgap material would be expected to perform a higher photocatalytic activity owing to a larger light absorption as compared to a wide bandgap material. However, the observation in present study exhibited a different effect, the phenomenon confirmed that other critical factors were dominating its photocatalytic performance in addition to light absorption.

To conduct the electronic structure of $Zn_{1-x}Cd_xS$ samples, the XAS analysis of sulfur K-edge and L-edge were performed. The feature A was assigned to a transitions from S 1s to 3p unoccupied final states (Figure 7a), and the other significant peak B at the L-edge corresponded to a transitions from S 2p to 3s states (Figure 7b).[42] The final states were consistent with the electric-dipole transition rule, in which S 3s and 3p state hybridized with Cd 5s or Zn 4s states provided the information about unoccupied states above the Fermi level as well as the bottom of the conduction band (CB).[43] These spectra exhibited a clear edge shift toward lower energy region with increasing the value of x, the shift in peak A was approximately 1.0 eV at the K-edge (from 2473.6 to 2472.6 eV) and that of peak B was approximately 1.2 eV at the L-edge (from 161.7 to 160.5 eV). The energy level of the conduction band minimum (CBM) declined once the Cd content (x) was increased, which was in agreement with the UV−vis absorption measurements. In addition, the peaks c1, c2 and c3 were observed in S L-edge spectra as shown in Figure 7b. Peak c1 at 167.3 eV was assigned to a transition from S 2p electrons to e states in zinc blende phase, while spin−orbit splitting of the S 2p states in wurtzite phase yielded c2 (166.4 eV) and c3 peaks (167.6 eV).[42] Noted that peak c1 in all samples was getting broader with increased Cd content, the broaden c1 peaks was due to the crystal distortion while peaks c2 and c3 became intense gradually ($x \geq 0.55$). These results indicated that zinc blende phase is the major phase in $Zn_{1-x}Cd_xS$ samples, whereas minor wurtzite phase appeared once half of the Zn ions were randomly replaced by Cd in $Zn_{1-x}Cd_xS$ ($x > 0.5$). This observation also supported the result from the Rietveld refinement (vide supra).

Figure 8a presented the near-edge features of the Zn K-edge XANES spectra for various Cd contents, where the main line in the photon energy 9650 to 9670 eV region corresponded to an electronic transition from the Zn 1s state to Zn 4p state, and no significant spectral change was observed. The Cd K-edge spectra in Figure 8b revealed that the transitions from Cd 1s levels to Cd 5p unoccupied state, these spectra exhibited a multipeak structure at photon energy of 26700 to 26750 eV. Since the signal was found to be sensitive to the presence of Cd ions and structural symmetry, the main feature of the Cd K-edge was observed to vary systematically with increasing Cd content, revealed that the local symmetry of this $Zn_{1-x}Cd_xS$ solid solution formed a new phase in addition to zinc blende phase. The Zn and Cd ions remained divalent since no significant edge shift was observed both in Zn and Cd K-edge XANES spectra, indicating that the oxidation states of those were identical. A variation in the local crystalline structure commonly influences the electronic properties in most systems including orbital splitting, valence states, and charge transfer, which means that an increase in bond length (Zn/Cd−S) considerably changes the density of states and therefore stability of the samples.

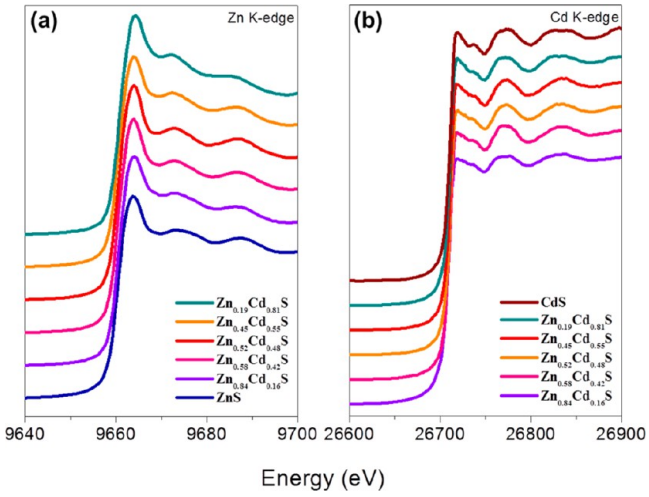

Figure 8. Near-edge features of (a) Zn and (b) Cd K-edge XANES Spectra of $Zn_{1-x}Cd_xS$ samples with x = 0, 0.16, 0.42, 0.48, 0.55, 0.81, and 1.

DOI: 10.1021/acsami.5b06872
ACS Appl. Mater. Interfaces 2015, 7, 22558−22569

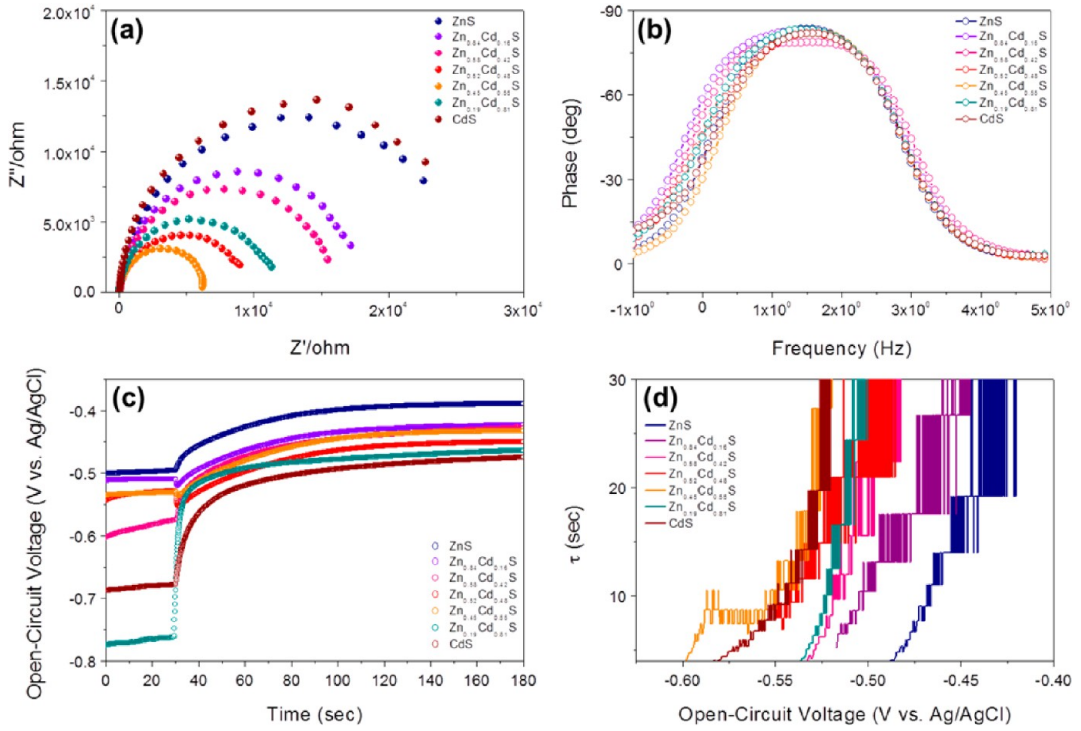

Figure 9. (a) Nyquist plots; (b) Bode plots of the EIS measurement; (c) Open-circuit voltage decay (OCVD) and (d) average electron lifetime calculated from VOC decay of various $Zn_{1-x}Cd_xS$ samples under the visible-light illumination.

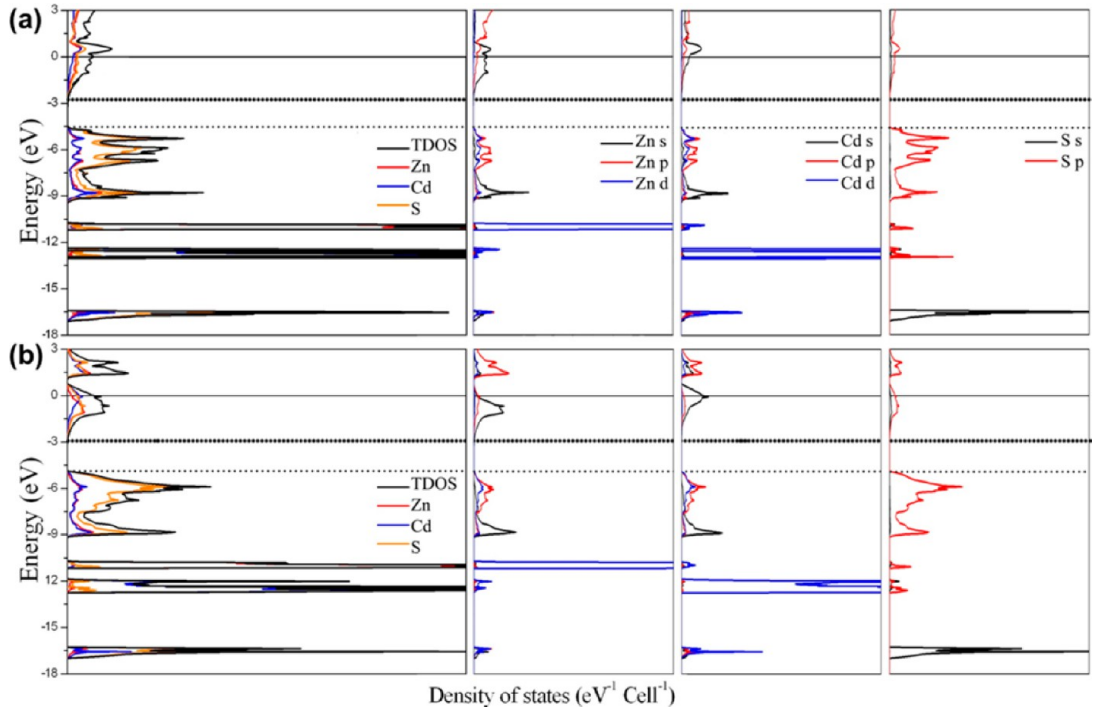

Figure 10. Calculated total density of states (DOS) and partial density of states (PDOS) curves for (a) zinc blende phase of $Zn_{0.5}Cd_{0.5}S$ and (b) wurtzite phase of $Zn_{0.5}Cd_{0.5}S$.

DISCUSSION

Photoelectrochemical Studies. EIS analysis are able to reveal the charge-transfer resistance at the interface of aggregate samples and the electron transport parameters (such as lifetime) can be calculated by fitting the Nyquist plots.[44] The Nyquist plots of the impedance data of $Zn_{1-x}Cd_xS$ samples are shown in Figure 9a, the charge-transfer resistance of $Zn_{0.45}Cd_{0.55}S$ rapidly decreased from 14k to 3k ohms, revealing a diminution in the electron recombination time. This can be attributed to the contribution of heterojunction which caused by zinc blende and wurtzite phases and further extend the electron lifetime efficiently. Besides, open-circuit voltage decay (OCVD) technique is a method that consists of cut off the

DOI: 10.1021/acsami.5b06872
ACS Appl. Mater. Interfaces 2015, 7, 22558−22569

illumination and monitoring the gradually decay of photovoltage (V_{OC}), and the lifetime of photocarriers could be extracted according to equation below:

$$\tau_n = -\frac{k_B T}{e}\left(\frac{dV_{oc}}{dt}\right)^{-1}$$

where k_B is the Boltznmann constant, T is temperature (K), e is electron charge, and V_{OC} is the open-circuit voltage. τ_n represents the lifetime of charge carriers.[45] It is obvious that the average lifetime assigned to the excited electron within the conducion band increased dramaticlly with existing of two phases (as shown in Figure 9d). However, CdS exhibited poor photocatalytic H_2 production even though it has longer electron lifetime as a result of higher wurtzite/zinc blende mixed phase ratio about 3.8. It can be attributed to the undesired photocorrosion of Cd−S bonding, which significantly decrease the photocatalytic performance.

Electronic Structure Calculation. To have a better understanding of the influence of Cd inclusion in $Zn_{1-x}Cd_xS$ series, the electronic structure including total/partial density of states (TDOS/PDOS) of ordered binary and ternary zinc blende phase ZnS. The electronic structure calculation of $Zn_{0.5}Cd_{0.5}S$ with wurtzite phase was also carried out and present side-by-side to $Zn_{0.5}Cd_{0.5}S$ with zinc blende phase in Figure 10. $Zn_{0.75}Cd_{0.25}S$, $Zn_{0.5}Cd_{0.5}S$, $Zn_{0.25}Cd_{0.75}S$ and CdS were computed on the basis of tight-binding linear-muffin-tin-orbital method (TB-LMTO) and shown in Figure S7. In Figure S7, the dot line and the dash line represent valence band (VB) and conduction band (CB), respectively. One can realize that the bandgap shrink gradually with increasing Cd content, which supported the UV−vis absorption results that the absorptions clearly red shift with higher amount of Cd in $Zn_{1-x}Cd_xS$ samples. In addition, the band gaps of $Zn_{1-x}Cd_xS$ in all cases are slightly smaller than those from UV−vis experiments. It is commonly seen in TB-LMTO calculation, which the LDA is implemented to deal with the exchange-correlation energy and no "derivative discontinuity" (DD) contribution was taken into account.[46] Below the Fermi level, there is a substantial overlapping of bands from Zn, Cd and S, which indicates strong bonding interactions between these elements. The electronic structure of zinc blende and wurtzite phases are more or less the same (Figure 10), the major contribution of these bands are mainly from the Zn 4s, 4p bands; Cd 5s, 5p bands and S 4p band. The conduction and valence bands of zinc blende phase are slightly higher than that of wurtzite phase. Therefore, one can recognize that between the heterojunction, the electrons in the CBs will flow from zinc blende phase to wurtzite phase and improve the charge separation (i.e., lower the possibility of electron−hole recombination).

Heterojunction Formation. Combining the structural (PXRD) and morphology (SEM and TEM) analyses mentioned above, one could realize that the synthesized $Zn_{1-x}Cd_xS$ samples could be a solid solution of zinc blende phase or mixed major zinc blende and minor wurtzite phases depending on the amount of Cd inclusion in the sample. The existence of two phases could form a heterojunction in the sample. A schematic representation of zinc blende and wurtzite phases of $Zn_{1-x}Cd_xS$ was shown in Figure 11a. In both phases, the Zn/Cd atoms connected to four S atoms to construct tetrahedral subunit ($[Zn/Cd]S_4$) and this subunit will further connect each other via sharing the corners to build the three-dimensional structures. Despite the way of the arrangement of

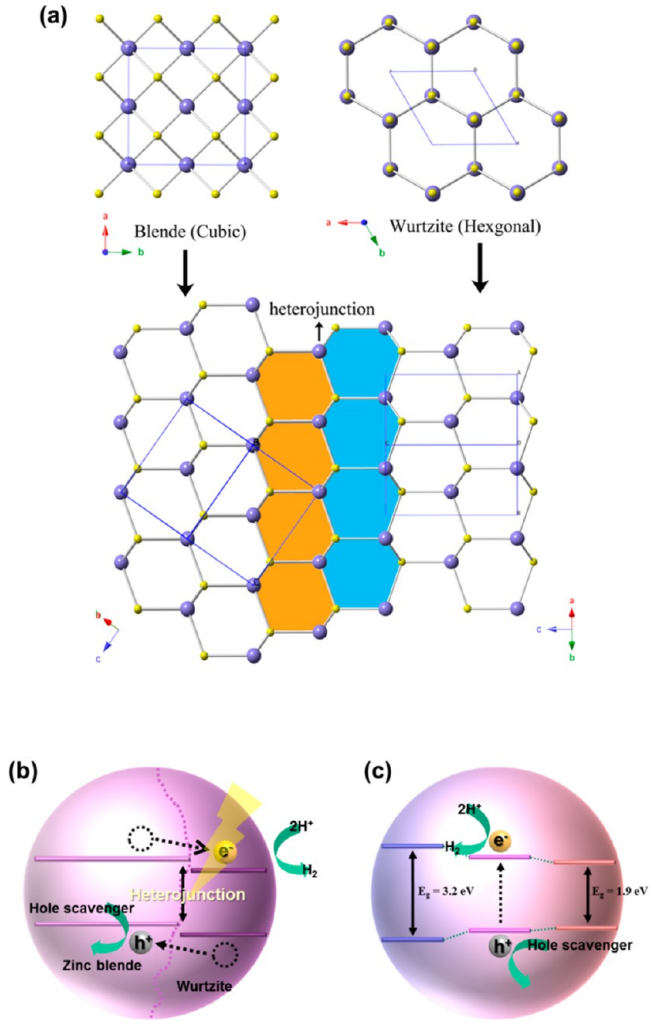

Figure 11. (a) Schematic representation of crystal structure of zinc blende and wurtzite phases for $Zn_{1-x}Cd_xS$ and heterojunction and schematic description of band structure alignments of the $Zn_{1-x}Cd_xS$ solid solution with (b) x = 0.48, 0.55, 0.81, and 1; (c) x = 0, 0.16, and 0.42.

$[Zn/Cd]S_4$ in both phases are slightly different, one can still adjust the orientation of these two phases to joint together to form heterojunctions (as indicated by the thinner arrow in Figure 11a). It has been suggested before that the heterojunctions would improve charge-hole separation and therefore enhance catalytic performance.[47]

Photocatalytic Enhancement. Various reports demonstrated that the high activity of $Zn_{1-x}Cd_xS$ solid solution with one phase could be attributed to the elevating of conduction band minimum (CBM) and narrowing bandgap. The conduction and valence band edges straddled with the redox potentials to increase the mobility of photogenerated holes and electrons while the band gap nonlinearly increased with increasing Zn content.[21,48,49] In order to obtain more efficient photocatalytic performance, the noble metals as cocatalysts was utilized to prohibit some shortcomings. The photogenerated electron and hole from $Zn_{1-x}Cd_xS$ is incorporating cocatalysts that could separate the photogenerated electron and hole into different parts of catalyst and thus suppress the electron−hole recombination.[37,50−52] In our case, the formation of heterojunction was able to separate the photogenerated charge-carriers more efficiently,[53,54] and an appropriate amount of

DOI: 10.1021/acsami.5b06872
ACS Appl. Mater. Interfaces 2015, 7, 22558−22569

$Zn_{1-x}Cd_xS$ sample with the x value of 0.55 showed the significantly highest photocatalytic activity. A schematic diagram was presented in Figure 11b and 11c to summarize the mechanism of photocatalytic reaction within the $Zn_{1-x}Cd_xS$ solid solution system. The electron microscope and X-ray diffraction results revealed that the majority of $Zn_{1-x}Cd_xS$ samples were zinc blende phase in all the case. It should note that the photocatalytic activity in this condition ($Zn_{0.45}Cd_{0.55}S$) was strongly dependent on the contribution from coexistence of zinc blende and wurtzite phases as show in Figure 11b. In the transfer process, the photogenerated electrons in the VB of $Zn_{1-x}Cd_xS$ solid solution could be excited to the CB and the same amount of holes were remained in the VB, which was applicable for both zinc blende phase and wurtzite phases. However, the Fermi level for a junction must align when the two materials are in equilibrium so that the electrons in the CB of zinc blende phase would diffuse into the CB of wurtzite phases. Meanwhile, the relative holes transferred from the VB of wurtzite to that of zinc blende phase driven by potential energy of Fermi level equilibration, which provides the information on the alignment of bands and the heterojunction of these interface as a result of better charge separation and prolonged lifetime for charge carriers.[55] Most importantly, heterojunctions were significantly generated and could lead to a spontaneous polarization within heterocrystal, which allows us to effectively separate the photogenerated electron−hole pairs. This spontaneous polarization greatly influenced the distribution of electrostatic potential and thus resulted in a localization of partial charge densities of valence band VBM and CBM, and thereby this effect was able to afford extra potential to promote the photocatalytic reaction for H_2 production.[56] Afterward, the photogenerated electrons in the CB of wurtzite phase would react with proton to form the hydrogen gas, which would collect to estimate the photocatalytic activity. In contrast, the holes in the VB of zinc blende phase would consumed by the scavenger. The improvement of photocatalytic activity also could be attributed to the formation of boundary between two crystalline phases that effectively separated the free charges to prevent their recombination.[57,58] However, the H_2 production was rapidly dropped in the case of $x > 0.55$ because of the presence of the undesired photocorrosion in Cd−S bonding. The decrement of heterojunction could be one of the reasons for deterioration of photocatalytic activity while Cd content was increasing, however; CdS sample exhibits a higher ratio of wurtzite/zinc blende phase (3.8) than that of $Zn_{0.18}Cd_{0.82}S$ sample (2.0), it still failed to produce H_2. As a result, this observation suggested that intrinsic nature of CdS was dominant reason, in which the undesired photocorrosion of Cd−S bonding might dominate the photocatalytic activity. The increment of Cd content caused more Cd−S bonding, which would expose to the electrolyte without the protection of Zn/Cd−S structure, this was obviously that bare CdS easily accepted the photogenerated holes and further covered into cadmium ion and sulfur during the photocatalytic reaction. By contrast, only the band structure bowing was obtained in the case of $Zn_{1-x}Cd_xS$ samples with zinc blende structure ($x < 0.48$).[19] The high photocatalytic efficiency of solid solution due to the balance of the CBM arising and the bandgap widening, in which neither P−N junction nor charge-carrier separation were generated (Figure 11c). As a result, several possible factors including band structure evolution, photocorrosion resistance, and heterojunction formation should be taken into account to promote the photocatalytic H_2 evolution of $Zn_{1-x}Cd_xS$ solid solution under visible-light irradiation in the present study.

CONCLUSIONS

In summary, the liquid phase coprecipitation method at low temperature allows us to synthesize $Zn_{1-x}Cd_xS$ solid solution with coexisted zinc blende and wurtzite phases and exhibit potential for photocatalytic H_2 evolution. A highest hydrogen production of 30 μmol h^{-1} mg^{-1} was observed and it was more than that of others ZnS-CdS nanocomposites even though the solid solution samples which reported in previous studies. Several strategies were utilized to elucidate the relationship between the photocatalytic efficiency and structural phase properties, whereas the electron microscope results demonstrated the existence of two phases. Moreover, the XANES of sulfur and UV−vis spectra illustrated that the narrow bandgap of $Zn_{1-x}Cd_xS$ solid solution extended into the visible light absorption region caused by mixing phases. Synchrotron X-ray absorption and diffraction spectroscopy were employed to establish the coexisted phase of zinc blende with minor wurtzite phase of $x \geq 0.48$. The heterojunction between boundaries can effectively separate the photogenerated electron−hole pairs and prevent their recombination to significantly promote the photocatalytic activity. This remarkable band structure and phase distribution of coexisting zinc blende/wurtzite phases can deliver a valuable enhancement effect in photoactivity than conventional $Zn_{1-x}Cd_xS$ solid solution during the high temperature process. This construction will clarify the mechanism of $Zn_{1-x}Cd_xS$ samples with lower temperature synthesis in the application of photocatalysis and H_2 production. Although $Zn_{1-x}Cd_xS$ system with mixed phase was used as a platform to explore the enhancement mechanism of heterojunction formation, we believe that our strategy is fundamental to the design of solar energy devices and should become an accepted concept in the photocatalytic system.

ASSOCIATED CONTENT

Supporting Information

The Supporting Information is available free of charge on the ACS Publications website at DOI: 10.1021/acsami.5b06872.

SXRD refinement results of $Zn_{1-x}Cd_xS$, SEM and TEM image of CdS, XRD results of $Zn_{1-x}Cd_xS$, Zn and DOS results of CdS in zinc blende and wurtzite (PDF)

AUTHOR INFORMATION

Corresponding Authors

*E-mail: clchen@phys.sinica.edu.tw.
*E-mail: chan.ts@nsrrc.org.tw.
*E-mail: haomingchen@ntu.edu.tw.

Author Contributions

The manuscript was written through contributions of all authors. All authors have given approval to the final version of the manuscript.

Notes

The authors declare no competing financial interest.

ACKNOWLEDGMENTS

We acknowledge support from the Ministry of Science and Technology, Taiwan (Contracts MOST 104-2113-M-213-001 and MOST 104-2113-M-002-011-MY2), and are grateful to Ms. Chia Ying Chien and Su Jen Ji of the Ministry of Science

DOI: 10.1021/acsami.5b06872
ACS Appl. Mater. Interfaces 2015, 7, 22558−22569

and Technology (National Taiwan University) for their assistance during the TEM and SEM experiments.

REFERENCES

(1) Fang, X. S.; Bando, Y.; Liao, M. Y.; Gautam, U. K.; Zhi, C. Y.; Dierre, B.; Liu, B. D.; Zhai, T. Y.; Sekiguchi, T.; Koide, Y.; Golberg, D. Single-Crystalline ZnS Nanobelts as Ultraviolet-Light Sensors. *Adv. Mater.* **2009**, *21* (20), 2034−2039.

(2) Zhai, T. Y.; Fang, X. S.; Bando, Y. S.; Liao, Q.; Xu, X. J.; Zeng, H. B.; Ma, Y.; Yao, J. N.; Golberg, D. Morphology-Dependent Stimulated Emission and Field Emission of Ordered CdS Nanostructure Arrays. *ACS Nano* **2009**, *3* (4), 949−959.

(3) Barea, E. M.; Shalom, M.; Gimenez, S.; Hod, I.; Mora-Sero, I.; Zaban, A.; Bisquert, J. Design of Injection and Recombination in Quantum Dot Sensitized Solar Cells. *J. Am. Chem. Soc.* **2010**, *132* (19), 6834−6839.

(4) Jing, D. W.; Guo, L. J. A Novel Method for the Preparation of a Highly Stable and Active CdS Photocatalyst with a Special Surface Nanostructure. *J. Phys. Chem. B* **2006**, *110* (23), 11139−11145.

(5) Janet, C. M.; Viswanath, R. P. Large Scale Synthesis of CdS Nanorods and Its Utilization in Photo-catalytic H_2 Production. *Nanotechnology* **2006**, *17* (20), 5271.

(6) Li, Q.; Guo, B. D.; Yu, J. G.; Ran, J. R.; Zhang, B. H.; Yan, H. J.; Gong, J. R. Highly Efficient Visible-Light-Driven Photocatalytic Hydrogen Production of CdS-Cluster-Decorated Graphene Nanosheets. *J. Am. Chem. Soc.* **2011**, *133* (28), 10878−10884.

(7) Zong, X.; Yan, H.; Wu, G.; Ma, G.; Wen, F.; Wang, L.; Li, C. Enhancement of Photocatalytic H_2 Evolution on CdS by Loading MoS_2 as Cocatalyst under Visible Light Irradiation. *J. Am. Chem. Soc.* **2008**, *130* (23), 7176−7177.

(8) Jia, L.; Wang, D. H.; Huang, Y. X.; Xu, A. W.; Yu, H. Q. Highly Durable N-Doped Graphene/CdS Nanocomposites with Enhanced Photocatalytic Hydrogen Evolution from Water under Visible Light Irradiation. *J. Phys. Chem. C* **2011**, *115* (23), 11466−11473.

(9) Yu, J.; Zhang, J.; Jaroniec, M. Preparation and Enhanced Visible-light Photocatalytic H_2-production Activity of CdS Quantum Dots-sensitized $Zn_{1-x}Cd_xS$ Solid Solution. *Green Chem.* **2010**, *12* (9), 1611−1614.

(10) Zhang, H.; Zhu, Y. F. Significant Visible Photoactivity and Antiphotocorrosion Performance of CdS Photocatalysts after Monolayer Polyaniline Hybridization. *J. Phys. Chem. C* **2010**, *114* (13), 5822−5826.

(11) Bao, N.; Shen, L.; Takata, T.; Domen, K. Self-Templated Synthesis of Nanoporous CdS Nanostructures for Highly Efficient Photocatalytic Hydrogen Production under Visible Light. *Chem. Mater.* **2008**, *20* (1), 110−117.

(12) Hu, J.-S.; Ren, L.-L.; Guo, Y.-G.; Liang, H.-P.; Cao, A.-M.; Wan, L.-J.; Bai, C.-L. Mass Production and High Photocatalytic Activity of ZnS Nanoporous Nanoparticles. *Angew. Chem., Int. Ed.* **2005**, *44* (8), 1269−1273.

(13) Cheon, J.; Zink, J. I. Gas Phase Photochemical Synthesis of II/VI Metal Sulfide Films and in Situ Luminescence Spectroscopic Identification of Photofragments. *J. Am. Chem. Soc.* **1997**, *119* (16), 3838−3839.

(14) Hsu, Y.-J.; Lu, S.-Y. Preparation of Nanosized ZnS-Passivated CdS Particle Films via the MOCVD Process with Co-fed Single Source Precursors. *Langmuir* **2004**, *20* (1), 194−201.

(15) Liu, Y.; Zapien, J. A.; Shan, Y. Y.; Geng, C. Y.; Lee, C. S.; Lee, S. T. Wavelength-Controlled Lasing in $Zn_xCd_{1-x}S$ Single-Crystal Nanoribbons. *Adv. Mater.* **2005**, *17* (11), 1372−1377.

(16) Zhong, X.; Han, M.; Dong, Z.; White, T. J.; Knoll, W. Composition-Tunable $Zn_xCd_{1-x}Se$ Nanocrystals with High Luminescence and Stability. *J. Am. Chem. Soc.* **2003**, *125* (28), 8589−8594.

(17) Zhong, X.; Feng, Y.; Knoll, W.; Han, M. Alloyed $Zn_xCd_{1-x}S$ Nanocrystals with Highly Narrow Luminescence Spectral Width. *J. Am. Chem. Soc.* **2003**, *125* (44), 13559−13563.

(18) Chen, H. M.; Chen, C. K.; Liu, R.-S.; Zhang, L.; Zhang, J.; Wilkinson, D. P. Nano-architecture and Material Designs for Water Splitting Photoelectrodes. *Chem. Soc. Rev.* **2012**, *41* (17), 5654−5671.

(19) Chen, H. M.; Chen, C. K.; Liu, R.-S.; Wu, C.-C.; Chang, W.-S.; Chen, K.-H.; Chan, T.-S.; Lee, J.-F.; Tsai, D. P. A New Approach to Solar Hydrogen Production: a ZnO-ZnS Solid Solution Nanowire Array Photoanode. *Adv. Energy Mater.* **2011**, *1* (5), 742−747.

(20) Maeda, K.; Takata, T.; Hara, M.; Saito, N.; Inoue, Y.; Kobayashi, H.; Domen, K. GaN:ZnO Solid Solution as a Photocatalyst for Visible-Light-Driven Overall Water Splitting. *J. Am. Chem. Soc.* **2005**, *127* (23), 8286−8287.

(21) Xing, C.; Zhang, Y.; Yan, W.; Guo, L. Band Structure-controlled Solid Solution of Photocatalyst for Hydrogen Production by Water Splitting. *Int. J. Hydrogen Energy* **2006**, *31* (14), 2018−2024.

(22) Reber, J. F.; Rusek, M. Photochemical Hydrogen Production with Platinized Suspensions of Cadmium Sulfide and Cadmium Zinc Sulfide Modified by Silver Sulfide. *J. Phys. Chem.* **1986**, *90* (5), 824−834.

(23) Li, Q.; Meng, H.; Zhou, P.; Zheng, Y. Q.; Wang, J.; Yu, J. G.; Gong, J. R. Zn1-xCdxS Solid Solutions with Controlled Bandgap and Enhanced Visible-Light Photocatalytic H_2-Production Activity. *ACS Catal.* **2013**, *3* (5), 882−889.

(24) Villoria, J. A.; Yerga, R. M. N.; Al-Zahrani, S. M.; Fierro, J. L. G. Photocatalytic Hydrogen Production on $Cd_{1-x}Zn_xS$ Solid Solutions under Visible Light: Influence of Thermal Treatment. *Ind. Eng. Chem. Res.* **2010**, *49* (15), 6854−6861.

(25) Wang, X.; Liu, G.; Chen, Z.-G.; Li, F.; Lu, G. Q.; Cheng, H.-M. Efficient and Stable Photocatalytic H_2 Evolution from Water Splitting by $(Cd_{0.8}Zn_{0.2})S$ Nanorods. *Electrochem. Commun.* **2009**, *11* (6), 1174−1178.

(26) Wang, L.; Wang, W. Z.; Shang, M.; Yin, W. Z.; Sun, S. M.; Zhang, L. Enhanced Photocatalytic Hydrogen Evolution under Visible Light over $Cd_{1-x}Zn_xS$ Solid Solution with Cubic Zinc Blend Phase. *Int. J. Hydrogen Energy* **2010**, *35* (1), 19−25.

(27) Wang, W. Z.; Zhu, W.; Xu, H. L. Monodisperse, Mesoporous $Zn_xCd_{1-x}S$ Nanoparticles as Stable Visible-Light-Driven Photocatalysts. *J. Phys. Chem. C* **2008**, *112* (43), 16754−16758.

(28) Chan, C. C.; Chang, C. C.; Hsu, C. H.; Weng, Y. C.; Chen, K. Y.; Lin, H. H.; Huang, W. C.; Cheng, S. F. Efficient and Stable Photocatalytic Hydrogen Production from Water Splitting over $Zn_xCd_{1-x}S$ Solid Solutions under Visible Light Irradiation. *Int. J. Hydrogen Energy* **2014**, *39* (4), 1630−1639.

(29) Zhang, L.; Li, Y. G.; Zhang, Q. H.; Wang, H. Z. Well-dispersed Pt Nanocrystals on the Heterostructured TiO_2/SnO_2 Nanofibers and the Enhanced Photocatalytic Properties. *Appl. Surf. Sci.* **2014**, *319*, 21−28.

(30) Guo, P. H.; Jiang, J. G.; Shen, S. H.; Guo, L. J. ZnS/ZnO Heterojunction as Photoelectrode: Type H Band Alignment towards Enhanced Photoelectrochemical Performance. *Int. J. Hydrogen Energy* **2013**, *38* (29), 13097−13103.

(31) Liu, M. C.; Wang, L. Z.; Lu, G. Q.; Yao, X. D.; Guo, L. J. Twins in $Cd_{1-x}Zn_xS$ Solid Solution: Highly Efficient Photocatalyst for Hydrogen Generation from Water. *Energy Environ. Sci.* **2011**, *4* (4), 1372−1378.

(32) Larson, A. C.; Von Dreele, R. B. *Generalized Structure Analysis System (GSAS)*; Los Alamos National Laboratory Report LAUR 86-478 ; Los Alamos National Laboratory: Los Alamos, NM, 1994.

(33) Shannon, R. D. Revised Effective Ionic Radii and Systematic Studies of Interatomic Distances in Halides and Chalcogenides. *Acta Crystallogr., Sect. A: Cryst. Phys., Diffr., Theor. Gen. Crystallogr.* **1976**, *32* (5), 751−767.

(34) Gorczyca, I.; Suski, T.; Christensen, N. E.; Svane, A. Size Effects in Band Gap Bowing in Nitride Semiconducting Alloys. *Phys. Rev. B: Condens. Matter Mater. Phys.* **2011**, *83* (15), No. 153301, DOI: 10.1103/PhysRevB.83.153301.

(35) Li, W. J.; Li, D. Z.; Chen, Z. X.; Huang, H. J.; Sun, M.; He, Y. H.; Fu, X. Z. High-efficient Degradation of Dyes by $Zn_xCd_{1-x}S$ Solid Solutions under Visible Light Irradiation. *J. Phys. Chem. C* **2008**, *112* (38), 14943−14947.

(36) Xu, X.; Hu, L.; Gao, N.; Liu, S.; Wageh, S.; Al-Ghamdi, A. A.; Alshahrie, A.; Fang, X. Controlled Growth from ZnS Nanoparticles to

DOI: 10.1021/acsami.5b06872
ACS Appl. Mater. Interfaces 2015, 7, 22558−22569

ZnS-CdS Nanoparticle Hybrids with Enhanced Photoactivity. *Adv. Funct. Mater.* **2015**, *25* (3), 445−454.
(37) Zeng, R. S.; Shen, R. G.; Zhao, Y. Q.; Li, X. S.; Sun, Z. G.; Shen, Y. Y. Aqueous Synthesis of Cu-doped ZnCdS/ZnS Core/shell Nanocrystals with a New and Highly Reactive Sulfur Source. *Nanotechnology* **2014**, *25* (13), 135602.
(38) Liu, J.; Zhang, D.; Pu, X.; Liu, J.; Zhang, R. Combustion Synthesis of $Zn_{1-x}Cd_xS$ and its Photodegradation Performance of Methylene Blue. *Mater. Lett.* **2014**, *117*, 158−161.
(39) Zhang, K.; Jing, D.; Xing, C.; Guo, L. Significantly Improved Photocatalytic Hydrogen Production Activity over Photocatalysts Prepared by a Novel Thermal Sulfuration Method. *Int. J. Hydrogen Energy* **2007**, *32* (18), 4685−4691.
(40) Bao, N.; Shen, L.; Takata, T.; Domen, K.; Gupta, A.; Yanagisawa, K.; Grimes, C. A. Facile Cd-Thiourea Complex Thermolysis Synthesis of Phase-Controlled CdS Nanocrystals for Photocatalytic Hydrogen Production under Visible Light. *J. Phys. Chem. C* **2007**, *111* (47), 17527−17534.
(41) Meissner, D.; Memming, R.; Kastening, B. Photoelectrochemistry of Cadmium-Sulfide 0.1. Reanalysis of Photocorrosion and Flat-Band Potential. *J. Phys. Chem.* **1988**, *92* (12), 3476−3483.
(42) Li, D.; Bancroft, G. M.; Kasrai, M.; Fleet, M. E.; Feng, X. H.; Tan, K. H.; Yang, B. X. Sulfur K- and L-edge XANES and Electronic Structure of Zinc, Cadmium and Mercury Monosulfides: a Comparative Study. *J. Phys. Chem. Solids* **1994**, *55* (7), 535−543.
(43) Wu, J. C.; Zheng, J. W.; Zacherl, C. L.; Wu, P.; Liu, Z. K.; Xu, R. Hybrid Functionals Study of Band Bowing, Band Edges and Electronic Structures of Cd1-xZnxS Solid Solution. *J. Phys. Chem. C* **2011**, *115* (40), 19741−19748.
(44) Park, K.; Zhang, Q. F.; Garcia, B. B.; Zhou, X. Y.; Jeong, Y. H.; Cao, G. Z. Effect of an Ultrathin TiO_2 Layer Coated on Submicrometer-Sized ZnO Nanocrystallite Aggregates by Atomic Layer Deposition on the Performance of Dye-Sensitized Solar Cells. *Adv. Mater.* **2010**, *22* (21), 2329−2332.
(45) Bisquert, J.; Zaban, A.; Greenshtein, M.; Mora-Seró, I. Determination of Rate Constants for Charge Transfer and the Distribution of Semiconductor and Electrolyte Electronic Energy Levels in Dye-Sensitized Solar Cells by Open-Circuit Photovoltage Decay Method. *J. Am. Chem. Soc.* **2004**, *126* (41), 13550−13559.
(46) Toher, C.; Filippetti, A.; Sanvito, S.; Burke, K. Self-Interaction Errors in Density-Functional Calculations of Electronic Transport. *Phys. Rev. Lett.* **2005**, *95* (14), 146402.
(47) Xu, F. Y.; Xiao, W.; Cheng, B.; Yu, J. G. Direct Z-scheme anatase/Rutile bi-phase Nanocomposite TiO_2 Nanofiber Photocatalyst with Enhanced Photocatalytic H-2-production Activity. *Int. J. Hydrogen Energy* **2014**, *39* (28), 15394−15402.
(48) Zhang, K.; Jing, D. W.; Xing, C. J.; Guo, L. J. Significantly Improved Photocatalytic Hydrogen Production Activity over $Cd_{1-x}Zn_xS$ Photocatalysts Prepared by a Novel Thermal Sulfuration Method. *Int. J. Hydrogen Energy* **2007**, *32* (18), 4685−4691.
(49) Huang, J.-D.; Liu, J.-Y.; Han, K.-L. Hybrid Functionals Studies of Structural and Electronic Properties of $Zn_xCd_{(1-x)}S$ and $(Zn_xCd_{1-x})(Se_xS_{1-x})$ Solid Solution Photocatalysts. *Int. J. Hydrogen Energy* **2012**, *37* (23), 17870−17881.
(50) Zhang, J.; Yu, J. G.; Jaroniec, M.; Gong, J. R. Noble Metal-Free Reduced Graphene Oxide-$Zn_xCd_{1-x}S$ Nanocomposite with Enhanced Solar Photocatalytic H-2-Production Performance. *Nano Lett.* **2012**, *12* (9), 4584−4589.
(51) Zhang, K.; Jing, D. W.; Chen, Q. Y.; Guo, L. J. Influence of Sr-doping on the Photocatalytic Activities of CdS-ZnS Solid Solution Photocatalysts. *Int. J. Hydrogen Energy* **2010**, *35* (5), 2048−2057.
(52) Zhang, X.; Jing, D.; Guo, L. Effects of Anions on the Photocatalytic H_2 Production Performance of Hydrothermally Synthesized Ni-doped $Cd_{0.1}Zn_{0.9}S$ Photocatalysts. *Int. J. Hydrogen Energy* **2010**, *35* (13), 7051−7057.
(53) Zhao, H.; Dong, Y.; Jiang, P.; Wu, X.; Wu, R.; Chen, Y. Facile Preparation of a ZnS/ZnO Nanocomposite for Robust Sunlight Photocatalytic H_2 Evolution from Water. *RSC Adv.* **2015**, *5* (9), 6494−6500.
(54) Xu, X. J.; Hu, L. F.; Gao, N.; Liu, S. X.; Wageh, S.; Al-Ghamdi, A. A.; Alshahrie, A.; Fang, X. S. Controlled Growth from ZnS Nanoparticles to ZnS-CdS Nanoparticle Hybrids with Enhanced Photoactivity. *Adv. Funct. Mater.* **2015**, *25* (3), 445−454.
(55) Lv, C.; Chen, G.; Sun, J.; Zhou, Y.; Fan, S.; Zhang, C. Realizing Nanosized Interfacial Contact via Constructing $BiVO_4/Bi_4V_2O_{11}$ Element-copied Heterojunction Nanofibres for Superior Photocatalytic Properties. *Appl. Catal., B* **2015**, *179*, 54−60.
(56) Zhou, Z.; Li, M.; Wu, P.; Guo, L. Revisiting the Zinc-Blende/Wurtzite Heterocrystalline Structure in CdS. *Adv. Condens. Matter Phys.* **2014**, *2014*, 7.
(57) Huang, F.; Banfield, J. F. Size-Dependent Phase Transformation Kinetics in Nanocrystalline ZnS. *J. Am. Chem. Soc.* **2005**, *127* (12), 4523−4529.
(58) Zhang, J.; Xu, Q.; Feng, Z.; Li, M.; Li, C. Importance of the Relationship between Surface Phases and Photocatalytic Activity of TiO_2. *Angew. Chem., Int. Ed.* **2008**, *47* (9), 1766−1769.

DOI: 10.1021/acsami.5b06872
ACS Appl. Mater. Interfaces 2015, 7, 22558−22569